Hindawi
Mathematical Problems in Engineering
Volume 2022, Article ID 9732083, 16 pages
https://doi.org/10.1155/2022/9732083

*Research Article*

# Nonlinear Mixed Convective Bidirectional Dynamics of Double Stratified Radiative Oldroyd-B Nanofluid Flow with Heat Source/Sink and Higher-Order Chemical Reaction

**Iftikhar Ahmad,[1] Muhammad Faisal,[1] K. Loganathan,[2] Muhammad Zaheer Kiyani,[1] and Ngawang Namgyel[3]**

[1]*Department of Mathematics, Azad Jammu & Kashmir University, Muzaffarabad 13100, Pakistan*
[2]*Department of Mathematics and Statistics, Manipal University Jaipur, Jaipur 303007, Rajasthan, India*
[3]*Jigme Namgyel Engineering College, Royal University of Bhutan, Dewathang, Bhutan*

Correspondence should be addressed to Muhammad Faisal; muhammad.faisal@ajku.edu.pk, K. Loganathan; loganathankaruppusamy304@gmail.com, and Ngawang Namgyel; ngawangnamgyel@jnec.edu.bt

Received 29 December 2021; Revised 27 January 2022; Accepted 22 April 2022; Published 23 May 2022

Academic Editor: Mohsan Hassan



Little is known in the literature about the concept of nonuniform heat source/sink and higher-order chemical reaction for the dynamics of Oldroyd-B nanoparticles. Therefore, the present article addresses the nonuniform heat source/sink and higher-order chemical reaction features in nonlinear mixed convection bidirectional MHD dynamics of Oldroyd-B nanoparticles with thermal radiation aspects through porous space. Stratification effects for both the temperature and concentration setups are also used in the mathematical model with the significance of random movement and thermodiffusion of nanoparticles. Shape-preserving transformations have been employed to convert the transport equations into solvable forms. An innovative analytical tactic, namely, homotopy analysis method, has been adopted to find the solution of the modeled problem. Behaviors of pertinent parameters on thermal and concentration profiles have been discussed through various graphs. Inspection of heat/mass transport against appropriate varieties of pertinent parameters has been made and explained physically. Thermal profile is augmented with the higher estimations of space and temperature-dependent heat source/sink links. Concentration profile is diminished with the augmentation of higher-order chemical reaction parameter. Sherwood number is improved with the estimation of $0 \le \beta_t \le 100$ and is reduced with the growth of $0 \le \beta_c \le 100$. Nusselt number is declined with the upgraded amounts of $0 \le N_b \le 3$ and $0 \le N_t \le 5$.

## 1. Introduction

Rheology of non-Newtonian fluids is based on their multiphase nature, and they have got great importance on account of their wide spread involvement in industrial and technological applications. Shear-thinning, shear thickening, and viscoelasticity are the main characteristics of non-Newtonian liquids. These characteristics are described by nonlinear relationship between shear force and shearing deformation. Several models of non-Newtonian materials have been suggested, like Maxwell, Jeffery, and Oldroyd-B models. An Oldroyd-B model is a rate type non-Newtonian material having relaxation and retardation time effects.

Thermal energy has a significant role in almost every field of science, engineering, industries, biomedicine, plant processing, transports, power houses, generating stations, and many others. The effectiveness of all the above cited applications is greatly dependent upon thermal conductivity of the fluids involved in the heat interchanging processes. Many fluids like water, ethylene, and oil bear the restrictions in applications due to low thermal conductivity. Hence, nanoparticles of average size of about 1–100 nm are inserted into the base fluid to augment the thermophysical and concentration circumstances of the fluid, and the obtained colloidal suspension is regarded as nanofluid. The novel attributes of nanofluids make them positively functional in

the numerous applications of heat transference along with microelectronics, energy cells, and domiciliary refrigeration and heating equipment, in disintegrating and cracking units, machining, hybrid powered engines, medications, and heat exchange units. Choi and Eastman [1] firstly proposed the term nanofluid through a permeable prolonging sheet along with consumption/injection. Then, Xuan and Li [2] extended the concept of nanofluids by proposing that fluids with solidified particles of metalloid and polymeric origin in a base fluid can also be termed as nanofluids. Buongiorno [3] formulated a mathematical tool for the analysis of convective transference in nanofluids with the consideration of Brownian movement and thermal diffusion properties. Copper, titanium, silicon, aluminum, zinc, magnesium, and graphene oxide are the best well-known particulates used for the development of nanofluids, while water, oil, glycol, and ethylene are the most regular working liquids.

Boundary-layer flows through stretching surfaces have been considered in studies because of their countless applications from household practices to aerospace such as in industries, irrigation waterways, environmental production, aerodynamics, sports, enhancement of heat transference, enhancement of mixing, transport of species, formation of rubber and plastic sheets, and fiber glass manufacturing. Boundary-layer flow produced by continuous elongation of obstacle was primarily studied by Sakiadis [4]. Crane [5] introduced the development of boundary-layer stream through stretching of surface and found exact solutions for the flow field. The bidirectional flow caused as a result of linearly plane bidirectional stretching of sheet was studied by Wang [6]. Ariel [7] deduced approximate analytical and numerical solutions of bidirectional steady flow over an elongating sheet. Sajid and Hayat [8] premeditated the aspects of thermal deposition and heat transportation in the boundary-layer dynamics of a viscid fluid influenced by an exponential elongation of obstacle. An analysis of the motion of a nanofluid produced by stretching of surface using connective model was developed by Khan and Pop [9].

Bhattacharyya and Layek [10] investigated the effects of chemically receptive solute convergence in magnetohydrodynamic boundary-layer stream. Ahmad et al. [11] continued the work accomplished by Liu and Anderson [12] by estimating the Darcy resistance impact and applied magnetic field. Stratification is a predominant phenomenon which has gained remarkable consideration because of its inclusion in the geophysical flows such as waterways, within lakes, oceans, ground-water supplies, warm energy stockpiling frameworks, and so on. A lot of researchers experimented with stratification with different effects. Ibrahim and Makinde [13] considered the doubly stratified boundary-regime flow of nanomaterials through an upright plate. Loganathan et al. [14] inspected the effect of second-order slip in a convective dynamic of an Oldroyd-B material with the aspects of chemical reaction and thermal radiation. Sandeep and Reddy [15] studied magnetohydrodynamic (MHD) flow having double stratified and cross diffusion aspects for an Oldroyd-B fluid. Waqas et al. [16] described the features of mixed convection progression of an Oldroyd-B nanomaterial via accumulating the impact of heat creation as well as heat/mass stratification.

The notion of heat production/consumption is convenient in many practices including heat disposal of atomic fuel wreckage, underground removal of radiative garbage substances, food storages, and disconnecting materials in packed bed reactors. In this way, nanocomposites have a capacity to assemble incident radiation. Turkyilmazoglu and Pop [17] explored the concurrent effects of heat and mass transport with thermal radiation through an unsteady nanomaterial progression. Rashidi et al. [18] analyzed the effect of second law of thermodynamics in magnetohydrodynamic dynamics of nanoliquid over a revolving disk. Moradi et al. [19] performed an analysis to check the effects of nanoparticles in Jeffery–Hamel flow. Makinde et al. [20] analyzed the buoyancy-driven dynamics of nanoliquid near a stagnated domain with connective boundary conditions. Mahanthesh et al. [21] worked toward approximate solution for the dynamics of an Oldroyd-B material with the significance of thermal deposition and heat consumption/generation impacting upon a nonlinearly expanding obstacle.

The subject of fluid motion with the involvement of porous medium has developed significantly in many fields of science and engineering like flow through water rocks, skin pronouncement, liquid purification processes, chemical trash, crude oil production, porous insulation, grain storage, mastic transport modeling, and underground removal of atomic waste. The interdependence of the voids in a porous medium permits certain liquids to flow through material. Ghosh and Sana [22] studied the time dependent dynamics of an Oldroyd-B material influenced by reformed sine pulses. Mukhopadhyay [23] considered and studied the time dependent heat transference and mixed connective dynamics produced by a penetrable stretching obstacle. The magnetohydrodynamic dynamics of tiny-sized nanoparticles passed over a permeable wedge is scrutinized by Kandasamy et al. [24]. Tripathy et al. [25] analyzed the impact of chemical reaction on magnetohydrodynamic free connective sheet over an upright moving plate through permeable material. Ali et al. [26] presented the analytical solution for flowing fluid through exponential stretching of permeable surface including heat flux in permeable medium utilizing homotopy analysis method (HAM). Goud [27] introduced the magnetohydrodynamic flow through an upright appendicular plate including radiation and chemical reaction effects through a permeable medium. Some more impactful scientific contributions related to the bidirectional dynamics of nanofluids with various mechanical and thermal aspects have been made by some researchers [28–36].

The above literature survey reveals that the study of non-Newtonian nanofluid performs a vital role in the industrial and engineering advancements. Moreover, a huge gap regarding the combined study of nonlinear aspects of mixed convection, chemical reaction, and heat consumption/generation is found during literature review. Hence, the novelty of present exploration is to discuss the steady dynamics of 3D radiative non-Newtonian (Oldroyd-B) nanofluid with the nonlinear aspects of mixed convection, chemical reaction, and heat source/sink. Additionally, significance of porous medium, magnetohydrodynamics, and double stratification has been addressed to

achieve the thermal engineering relevancy of the mathematical model. To the best of our knowledge, no such attempt has been made previously. Mathematical modeling of the physical model has been completed with the help of boundary-layer approximations and basic laws of fluid dynamics. With the functionality of similarity transformations, transport equations have been converted into one parameter family of solvable equations based on the physical domain. Analytical analysis of the mathematical model has been presented by following the procedure of homotopy analysis method [37–44]. Some more solution techniques (Keller-Box method, Lie group analysis, etc.) have also been offered by some researchers/scholars [45–50], but here preference is given to homotopy analysis method because of its compatibility with the modeled problem. Finally, the obtained outcomes have been discussed physically with the support of various charts and tables against the fluctuating choices of involved parameters.

## 2. Model Development

An incompressible, doubly stratified, and three-dimensional steady dynamic of radiative Oldroyd-B magneto-nanomaterial impacting upon an expanding obstacle through porous space is considered with the nonlinear aspects of mixed convection, chemical reaction, and heat consumption/generation. Effects of random motion and thermodiffusion of nanoparticles have also been provided via Buongiorno nanofluid model. The Lorentz force is perpendicular to the $xy$-plane, whereas gravitational force is parallel to the $x$-direction. Influence of chemical reaction has been included in the nanoparticle mass transport equation, whereas radiation effects have been involved in the heat equation of the nanofluid. The expansion velocity along $x$-direction is explained as $u_w = ax$, whereas expansion velocity along the $y$-direction is elaborated as $v_w = by$. The relations for wall and free stream temperatures are settled according to the rule of thermal stratification, whereas the relations for wall and free stream nanoparticle mass concentration are established according to the regulation of solutal stratification. The graphical abstract of the present investigation is presented via Figure 1. The governing equations for the present analysis supported by [16, 22, 27, 31, 32, 44] are composed as

$$\frac{\partial u}{\partial x}+\frac{\partial v}{\partial y}+\frac{\partial w}{\partial z}=0, \tag{1}$$

$$\begin{aligned} u\frac{\partial u}{\partial x}+v\frac{\partial u}{\partial x}+w\frac{\partial u}{\partial z}+\lambda_1\left(\begin{array}{c} u^2\dfrac{\partial^2 u}{\partial x^2}+v^2\dfrac{\partial^2 u}{\partial y^2}+w^2\dfrac{\partial^2 u}{\partial z^2} \\ +2uv\dfrac{\partial^2 u}{\partial x\partial y}+2vw\dfrac{\partial^2 u}{\partial y\partial z}+2uw\dfrac{\partial^2 u}{\partial x\partial z}\end{array}\right), \\ =\vartheta\frac{\partial^2 u}{\partial z^2}+\vartheta\lambda_2\left(\begin{array}{c} u\dfrac{\partial^3 u}{\partial x\partial z^2}+v\dfrac{\partial^3 u}{\partial x\partial z^2}+w\dfrac{\partial^3 u}{\partial z^3} \\ -\dfrac{\partial u}{\partial x}\dfrac{\partial^2 u}{\partial z^2}-\dfrac{\partial u}{\partial y}\dfrac{\partial^2 u}{\partial z^2}-\dfrac{\partial u}{\partial z}\dfrac{\partial^2 w}{\partial z^2}\end{array}\right), \\ +g\left[\alpha_1\left(T-T_\infty\right)+\alpha_2\left(T-T_\infty\right)^2\right] \\ +g\left[\alpha_3\left(C-C_\infty\right)+\alpha_4\left(C-C_\infty\right)^2\right]-\frac{\mu_f\phi_1}{\rho_f p_1}u-\frac{\sigma B^{\circ 2}}{\rho_f}\left(u+\lambda_1 w\frac{\partial u}{\partial z}\right), \end{aligned} \tag{2}$$

$$\begin{aligned} u\frac{\partial v}{\partial x}+v\frac{\partial v}{\partial y}+w\frac{\partial v}{\partial z}+\lambda_1\left(\begin{array}{c} u^2\dfrac{\partial^2 v}{\partial x^2}+v^2\dfrac{\partial^2 v}{\partial y^2}+w^2\dfrac{\partial^2 v}{\partial z^2} \\ +2uv\dfrac{\partial^2 v}{\partial x\partial y}+2vw\dfrac{\partial^2 v}{\partial y\partial z}+2uv\dfrac{\partial^2 v}{\partial x\partial z}\end{array}\right), \\ =\vartheta\frac{\partial^2 v}{\partial z^2}+\vartheta\lambda_2\left(\begin{array}{c} u\dfrac{\partial^3 v}{\partial x\partial z^2}+v\dfrac{\partial^3 v}{\partial x\partial z^2}+w\dfrac{\partial^3 v}{\partial z^3} \\ -\dfrac{\partial v}{\partial x}\dfrac{\partial^2 v}{\partial z^2}-\dfrac{\partial v}{\partial y}\dfrac{\partial^2 v}{\partial z^2}-\dfrac{\partial v}{\partial z}\dfrac{\partial^2 w}{\partial z^2}\end{array}\right), \\ -\frac{\mu_f\phi_1}{\rho_f p_1}v-\frac{\sigma B^{\circ 2}}{\rho_f}\left(v+\lambda_1 w\frac{\partial v}{\partial z}\right), \end{aligned} \tag{3}$$

$$u\frac{\partial T}{\partial x}+v\frac{\partial T}{\partial y}+w\frac{\partial T}{\partial z}=\alpha_m\frac{\partial^2 T}{\partial z^2}$$
$$+\frac{(\rho c)_p}{(\rho c)_f}\left(D_B\left(\frac{\partial T}{\partial z}\frac{\partial C}{\partial z}\right)+\frac{D_T}{T_\infty}\left(\frac{\partial T}{\partial z}\right)^2\right)-\frac{1}{(\rho c)_f}\frac{\partial q_r}{\partial z}+\frac{q'''}{(\rho c)_f}, \tag{4}$$

$$u\frac{\partial C}{\partial x}+v\frac{\partial C}{\partial y}+w\frac{\partial C}{\partial z}=D_B\frac{\partial^2 C}{\partial z^2}+\frac{D_T}{T_\infty}\left(\frac{\partial^2 T}{\partial z^2}\right)$$
$$-\left[k_{c1}(C-C_\infty)+k_{c2}(C-C_\infty)^2\right]. \tag{5}$$

Here, $q''' = (ku_w/x\vartheta)[A^*(T_w - T_\infty)f' + B^*(T - T_\infty)]$.

The relevant boundary conditions supported by [15, 16, 44] are

$$u = u_w, v = v_w, w = 0, T = T_w, C = C_w \text{ at } z = 0,$$
$$u \longrightarrow 0, v \longrightarrow 0, T \longrightarrow T_\infty, C \longrightarrow C_\infty \text{ as } z \longrightarrow \infty. \tag{6}$$

Using the relation of Rosseland approximation, radiative heat-flux $q_r$ is determined as (see [48]) $q_r = -(4\sigma^*/3K^*)(\partial T^4/\partial z)$ with $T^4 \cong 4T_\infty^3 T - 3T_\infty^4$.

Here, $x$, $y$, and $z$ describe the space coordinates; $u$, $v$, and $w$ express parts of velocity in the direction of $x$, $y$, and $z$, respectively; $\lambda_1$ and $\lambda_2$ are used to represent relaxation time and retardation time, respectively; $\vartheta = (\mu_f/\rho_f)$ denotes kinematic viscosity with $\mu_f$ as dynamic viscosity and $\rho_f$ as density; $g$ represents the gravitational acceleration; $\alpha_1$ exhibits the involvement of linear thermal expansion; $\alpha_2$ represent involvement of nonlinear thermal expansion; $\alpha_3$ and $\alpha_4$ depict, respectively, linear and nonlinear concentration coefficients; $\sigma^*$ denotes Stefan–Boltzmann constant; $B_0$ stands for magnetic field strength with electrical conductivity $\sigma$; $\phi_1$ is used to express the porosity constant; $p_1$ the permeability constant; $T$ is the temperature, $C$ is the concentration of nanoparticles; $\alpha_m = (k/(\rho c)_f)$ denotes the thermal diffusivity with thermal conductivity $k$; and $D_B$ and $D_T$ are the symbols of random and thermodiffusion coefficients of nanocomposites, respectively. Efficient heat capability of nanoparticles and efficient heat capability of the fluid are symbolized by $(c)_p$ and $(c)_f$, respectively; $k_{c1}$ and $k_{c2}$ represent the first- and second-order chemical reaction parameters, respectively; $q_r$ is thermal deposition; $q'''$ is nonuniform heat consumption/absorption; $T_w$ is temperature at the surface; $T_\infty$ denotes the ambient temperature; and $C_w$ and $C_\infty$ serve as nanoparticle concentrations at the obstacle and far from the obstacle. Here, the expansion velocities, temperature, and nanoparticle mass concentration at the surface are described as (see [15, 16, 44])

$$\begin{aligned} u_w(x) &= ax,\\ v_w(y) &= by,\\ T_w(x) &= T_{\infty,0} + M_1 x,\\ C_w(x) &= C_{\infty,0} + N_1 x,\\ T_\infty(x) &= T_{\infty,0} + A_1 x,\\ C_\infty(x) &= C_{\infty,0} + B_1 x. \end{aligned} \tag{7}$$

Here, $a, b, A_1, B_1, M_1, N_1, T_{\infty,0}$, and $C_{\infty,0}$ are dimensional constants.

We utilize the accompanying similarity transformations supported by [37, 38, 44] as follows:

$$\left.\begin{aligned} &u = axf'(\eta), v = ayg'(\eta) \quad w = -(a\vartheta)^{1/2}(f+g), \eta = \left(\frac{a}{\vartheta}\right)^{1/2} z\\ &\theta(\eta) = \frac{T - T_{\infty,0}}{T} - \frac{A_1 x}{T} \quad \Delta T = T_w(x) - T_{\infty,0} = M_1 x\\ &\phi(\eta) = \frac{C - C_{\infty,0}}{C} - \frac{B_1 x}{C} \quad \Delta C = C_w(x) - C_{\infty,0} = N_1 x \end{aligned}\right\}. \tag{8}$$

Via using the above-mentioned local similarity set, (1) is straightforwardly fulfilled and simplified forms of (2-5) are mentioned below:

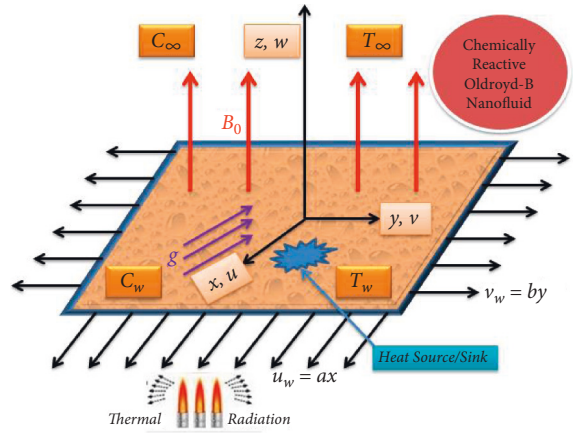


Figure 1: Graphical abstract of the mathematical model.

$$f''' + \left(1 + M^2\beta_1\right)(f+g)f'' - f'^2 + \beta_1\left[2(f+g)f'f'' - (f+g)^2 f'''\right], \\ + \beta_2\left[2(f''+g'')f'' - (f+g)f^{iv}\right] - \left(\delta + M^2\right)f' + \lambda\left[(1+\beta_t\theta)\theta + N^*(1+\beta_c\phi)\phi\right] = 0, \tag{9}$$

$$g''' + \left(1 + M^2\beta_1\right)(f+g)g'' - g'^2 + \beta_1\left[2(f+g)g'g'' - (f+g)^2 g'''\right], \\ + \beta_2\left[2(f''+g'')g'' - (f+g)g^{iv}\right] - \left(\delta + M^2\right)g' = 0, \tag{10}$$

$$\left(1 + \frac{4}{3}R_d\right)\theta'' + \Pr\left[(f+g)\theta' - (\theta+\varepsilon_t)f' + N_b\theta'\phi' + N_t\theta'^2\right] + A^*(1-\varepsilon_t)f' + B^*\theta = 0, \tag{11}$$

$$\phi'' + \Pr Le\left[(f+g)\phi' - (\phi+\varepsilon_s)f' - \gamma(1+k_c\phi)\phi\right] + \frac{N_t}{N_b}\theta'' = 0. \tag{12}$$

The boundary conditions are confined as

$$\begin{aligned} f &= 0, \\ g &= 0, \\ f' &= 1, \\ g' &= \alpha, \\ \theta &= 1 - \varepsilon_t, \\ \phi &= 1 - \varepsilon_s \text{ at } \eta = 0, \end{aligned} \tag{13}$$

$$\begin{aligned} f' &\longrightarrow 0, \\ g' &\longrightarrow 0, \\ f'' &\longrightarrow 0, \\ g'' &\longrightarrow 0, \\ \theta &\longrightarrow 0, \\ \phi &\longrightarrow 0, \text{ as } \eta \longrightarrow \infty. \end{aligned} \tag{14}$$

In the above-mentioned equations, $f'$ and $g'$ are the dimensionless velocities along $x$- and $y$-direction, respectively; $\theta$ and $\phi$ are the dimensionless temperature and concentration, respectively; $\beta_1 = \lambda_1 a$ and $\beta_2 = \lambda_2 a$ are the Deborah numbers corresponding to relaxation and retardation times, respectively; $\beta_t = (\alpha_2/\alpha_1)T$ and $\beta_c = (\alpha_4/\alpha_3)C$ indicate the nonlinear convection constraints for temperature and concentration, respectively; $M^2 = (\sigma B^{\circ}{}_2/\rho_f a)$ is the magnetic constraint; $\delta = (\vartheta\phi_1/p_1 a)$ is used to express the porosity constraint; $N^* = (\lambda^*/\lambda)$ stands for buoyancy ratio parameter; $\lambda = (Gr/Re_x^2)$ and $\lambda^* = (Gr^*/Re_x^2)$ denote the mixed convective parameters for thermal and concentration setups, respectively; $Le = (\alpha_m/D_B)$ is the Lewis number; $Pr = (\vartheta/\alpha_m)$ signifies the Prandtl number; $N_b = ((\rho c)_p/(\rho c)_f)(D_B\Delta C/\vartheta)$ denotes the random movement involvement; $N_t = ((\rho c)_p/(\rho c)_f)(D_T\Delta T/\vartheta T_\infty)$ corresponds to thermo-diffusion parameter; $A^*$ and $B^*$ denote, respectively, the quantities of space-dependent and temperature-dependent heat consumption/generation; $\gamma = (k_{c1}/a)$ is the rate of chemical reaction; $k_c = (k_{c2}/k_{c1})C$ is the dimensionless chemical reaction parameter; $R_d = (4T_\infty^3\sigma^*/kk^*)$ represents radiation parameter; $k^*$ represents the Rosseland mean absorption constant; $\alpha = (b/a)$ is the expansion ratio parameter; $\varepsilon_t = (A_1/M_1)$ and $\varepsilon_s = (B_1/N_1)$ are the representatives of the heat and mass stratified parameters, respectively; and prime represents differentiation taking $\eta$ as an independent similarity variable.

The amount of mass transference is presented by local Sherwood number $Sh_x$ while the amount of heat

transference is described by local Nusselt number $Nu_x$, and these numbers can be expressed in the form of Reynolds number $Re_x = (u_w x/\vartheta)$ as below:

$$\begin{aligned} Sh_x &= -\frac{x}{(C_w - C_\infty)}\frac{\partial C}{\partial z}\Big|_{z=0}, \\ &= -(Re_x)^{(1/2)}\phi'(0), \\ Nu_x &= -\frac{x}{(T_w - T_\infty)}\left(\frac{\partial T}{\partial z} - \frac{q_r}{k}\right)\Big|_{z=0}, \\ &= -(Re_x)^{(1/2)}\left(1 + \frac{4}{3}R_d\right)\theta'(0). \end{aligned} \tag{15}$$

## 3. Homotopic Series Solution

This section deals with the series solutions of the mathematical modeled dimensionless equations (9)–(12) based on boundary restrictions via (8) and (9) with the procedure of homotopy analysis method (HAM). For this purpose, primary guesses are approximated in accordance with boundary conditions (8) and (9) and are shown as

$$\begin{aligned} f_0(\eta) &= 1 - e^{-\eta}, \\ g_0(\eta) &= \alpha(1 - e^{-\eta}), \\ \theta_0(\eta) &= (1 - \varepsilon_t)e^{-\eta}, \\ \phi_0(\eta) &= (1 - \varepsilon_c)e^{-\eta}. \end{aligned} \tag{16}$$

The linear operators are denoted by $\mathscr{L}_f, \mathscr{L}_g, \mathscr{L}_\theta$, and $\mathscr{L}_\phi$ as follows:

$$\begin{aligned} \mathscr{L}_f &= f''' - f', \\ \mathscr{L}_g &= g''' - g', \\ \mathscr{L}_\theta &= \theta'' - \theta', \\ \mathscr{L}_\phi &= \phi'' - \phi', \\ &\left.\begin{aligned} \mathscr{L}_f[C_1 + C_2 e^{\eta} + C_3 e^{-\eta}] = 0 \quad \mathscr{L}_g[C_4 + C_5 e^{\eta} + C_6 e^{-\eta}] = 0 \\ \mathscr{L}_\theta[C_7 e^{\eta} + C_8 e^{-\eta}] = 0 \qquad \mathscr{L}_\phi[C_9 e^{\eta} + C_{10} e^{-\eta}] = 0 \end{aligned}\right\}, \end{aligned} \tag{17}$$

$$\begin{aligned} (1-P)\mathscr{L}_f\left[\widehat{f}(\eta,P) - f_0(\eta)\right] &= P\hbar_f \mathscr{N}_f[\widehat{f}(\eta,P), \widehat{g}(\eta,P), \widehat{\theta}(\eta,P), \widehat{\phi}(\eta,P)], \\ (1-P)\mathscr{L}_g\left[\widehat{g}(\eta,P) - g_0(\eta)\right] &= P\hbar_g \mathscr{N}_g[\widehat{f}(\eta,P), \widehat{g}(\eta,P), \widehat{\theta}(\eta,P), \widehat{\phi}(\eta,P)], \\ (1-P)\mathscr{L}_\theta\left[\widehat{\theta}(\eta,P) - \theta_0(\eta)\right] &= P\hbar_\theta \mathscr{N}_\theta[\widehat{f}(\eta,P), \widehat{g}(\eta,P), \widehat{\theta}(\eta,P), \widehat{\phi}(\eta,P)], \\ (1-P)\mathscr{L}_\phi\left[\widehat{\phi}(\eta,P) - \phi_0(\eta)\right] &= P\hbar_\phi \mathscr{N}_\phi[\widehat{f}(\eta,P), \widehat{g}(\eta,P), \widehat{\theta}(\eta,P), \widehat{\phi}(\eta,P)]. \end{aligned}$$

In the above relations, $\hbar_f$, $\hbar_g$, $\hbar_\theta$, and $\hbar_\phi$ are auxiliary constraints, whereas $\mathscr{N}_f$, $\mathscr{N}_g$, $\mathscr{N}_\theta$, and $\mathscr{N}_\phi$ serve as nonlinear operators, and $P$ is the embedding parameter. The BCs (boundary conditions) in the coding language can be expressed as

$$\left.\begin{aligned} &\widehat{f}(0,P) = 0,\ \widehat{f}'(0,P) = 1,\ \widehat{f}'(\infty,P) = 0,\ \widehat{g}(0,P) = 0,\ \widehat{g}'(0,P) = \alpha, \\ &\widehat{g}'(\infty,P) = 0,\ \widehat{\theta}(0,P) = 1 - \varepsilon_t,\ \widehat{\theta}(\infty,P) = 0,\ \widehat{\phi}(0,P) = 1 - \varepsilon_c,\ \widehat{\phi}(\infty,P) = 0 \end{aligned}\right\}, \tag{18}$$

$$\begin{aligned} \mathscr{N}_f[\widehat{f}(\eta,P), \widehat{g}(\eta,P), \widehat{\theta}(\eta,P), \widehat{\phi}(\eta,P)] &= \frac{\partial^3 \widehat{f}}{\partial \eta^3} + \left(1 + M^2 * \beta_1\right)(\widehat{f} + \widehat{g})\frac{\partial^2 \widehat{f}}{\partial \eta^2} - \left(\frac{\partial \widehat{f}}{\partial \eta}\right)^2, \\ +\beta_1\left(2(\widehat{f} + \widehat{g})\frac{\partial \widehat{f}}{\partial \eta}\frac{\partial^2 \widehat{f}}{\partial \eta^2} - (\widehat{f} + \widehat{g})^2\frac{\partial^3 \widehat{f}}{\partial \eta^3}\right) + \beta_2\left(2\left(\frac{\partial^2 \widehat{f}}{\partial \eta^2} + \frac{\partial^2 \widehat{g}}{\partial \eta^2}\right)\frac{\partial^2 \widehat{f}}{\partial \eta^2} - (\widehat{f} + \widehat{g})\frac{\partial^4 \widehat{f}}{\partial \eta^4}\right) - \left(\delta + M^2\right)\frac{\partial \widehat{f}}{\partial \eta}, \\ +\lambda\left[\left(\left(1 + \beta_t\widehat{\theta}\right)\widehat{\theta} + N^*\left(1 + \beta_t\widehat{\phi}\right)\widehat{\phi}\right)\right], \end{aligned} \tag{19}$$

$$\mathcal{N}_g[\widehat{f}(\eta,P),\widehat{g}(\eta,P),\widehat{\theta}(\eta,P),\widehat{\phi}(\eta,P)] = \frac{\partial^3\widehat{g}}{\partial\eta^3} + \left(1+M^2\beta_1\right)(\widehat{f}+\widehat{g})\frac{\partial^2\widehat{g}}{\partial\eta^2} - \left(\frac{\partial\widehat{g}}{\partial\eta}\right)^2,$$
$$+\beta_1\left(2(\widehat{f}+\widehat{g})\frac{\partial\widehat{g}}{\partial\eta}\frac{\partial^2\widehat{g}}{\partial\eta^2} - (\widehat{f}+\widehat{g})^2\frac{\partial^3\widehat{g}}{\partial\eta^3}\right) + \beta_2\left(2\left(\frac{\partial^2\widehat{f}}{\partial\eta^2}+\frac{\partial^2\widehat{g}}{\partial\eta^2}\right)\frac{\partial^2\widehat{g}}{\partial\eta^2} - (\widehat{f}+\widehat{g})\frac{\partial^4\widehat{g}}{\partial\eta^4}\right) - \left(\delta+M^2\right)\frac{\partial\widehat{g}}{\partial\eta}, \tag{20}$$

$$\mathcal{N}_\theta[\widehat{f}(\eta,P),\widehat{g}(\eta,P),\widehat{\theta}(\eta,P),\widehat{\phi}(\eta,P)] = \left(1+\frac{4}{3}R_d\right)\frac{\partial^2\widehat{\theta}}{\partial\eta^2} + Pr(\widehat{f}+\widehat{g})\frac{\partial\widehat{\theta}}{\partial\eta},$$
$$-Pr\left(\widehat{\theta}+\varepsilon_t\right)\frac{\partial\widehat{f}}{\partial\eta} + Pr*N_b\frac{\partial\widehat{\theta}}{\partial\eta}\frac{\partial\widehat{\phi}}{\partial\eta} + Pr*N_t\left(\frac{\partial\widehat{\theta}}{\partial\eta}\right)^2 + A^*\left(1-\varepsilon_t\right)\frac{\partial\widehat{f}}{\partial\eta} + B^*\widehat{\theta}, \tag{21}$$

$$\mathcal{N}_\phi[\widehat{f}(\eta,P),\widehat{g}(\eta,P),\widehat{\theta}(\eta,P),\widehat{\phi}(\eta,P)] = \frac{\partial^2\widehat{\phi}}{\partial\eta^2} + Le*Pr(\widehat{f}+\widehat{g})\frac{\partial\widehat{\phi}}{\partial\eta},$$
$$-Le*Pr\left(\widehat{\phi}+\varepsilon_c\right)\frac{\partial\widehat{f}}{\partial\eta} - Le*Pr*\gamma\widehat{\phi} - Le*Pr*\gamma*k_c\widehat{\phi}^2 + \left(\frac{N_t}{N_b}\right)\frac{\partial^2\widehat{\theta}}{\partial\eta^2}, \tag{22}$$

$$\mathcal{L}_f\left[f_m(\eta) - \chi_m f_{m_{-1}}(\eta)\right] = \hbar_f R_f^m(\eta), \tag{23}$$

$$\mathcal{L}_g\left[g_m(\eta) - \chi_m g_{m_{-1}}(\eta)\right] = \hbar_g R_g^m(\eta), \tag{24}$$

$$\mathcal{L}_\theta\left[\theta_m(\eta) - \chi_m\theta_{m_{-1}}(\eta)\right] = \hbar_\theta R_\theta^m(\eta), \tag{25}$$

$$\mathcal{L}_\phi\left[\phi_m(\eta) - \chi_m\phi_{m_{-1}}(\eta)\right] = \hbar_\phi R_\phi^m(\eta), \tag{26}$$

$$\begin{aligned} f_m(0) &= f_m'(0), \\ &= f_m'(\infty), \\ &= 0, \\ g_m(0) &\\ &= g_m'(\infty), \\ &= 0, \end{aligned} \tag{27}$$

$$\begin{aligned} \theta_m(0) &= \theta_m(\infty), \\ &= 0, \\ \phi_m(0) &= \phi_m(\infty), \\ &= 0, \end{aligned} \tag{28}$$

$$R_f^m(\eta) = f_{m-1}''(\eta) + \left(1+M^2\beta_1\right)\sum_{k=0}^{m-1}\left(f_{m-1-k}f_k'' + g_{m-1-k}f_k''\right) - \sum_{k=0}^{m-1}\left(f_{m-1-k}' + f_k'\right),$$
$$+2\beta_1\sum_{k=0}^{m-1}f_{m-1-k}\sum_{l=0}^{k}f_{k-1}'f_l'' + 2\beta_1\sum_{k=0}^{m-1}g_{m-1-k}\sum_{l=0}^{k}f_{k-1}'f_l'' - \beta_1\sum_{k=0}^{m-1}f_{m-1-k}''\sum_{l=0}^{k}f_{k-1}f_l,$$
$$-\beta_1\sum_{k=0}^{m-1}f_{m-1-k}''\sum_{l=0}^{k}g_{k-1}g_l - \sum_{k=0}^{m-1}f_{m-1-k}''\sum_{l=0}^{k}g_{k-1}f_l + 2\beta_1\sum_{k=0}^{m-1}f_{m-1-k}''f_k'' + 2\beta_1\sum_{k=0}^{m-1}g_{m-1-k}''f_k'', \tag{29}$$
$$-\beta_2\sum_{k=0}^{m-1}f_{m-1-k}f_k''' - \beta_2\sum_{k=0}^{m-1}g_{m-1-k}f_k''' - \left(\delta+M^2\right)f_{m-1}(\eta),$$
$$+\lambda\left(\theta_{m-1}(\eta) + \beta_t\sum_{k=0}^{m-1}\theta_{m-1-k}\theta_k + N*\phi_{m-1}(\eta) + N**\beta_c\sum_{k=0}^{m-1}\phi_{m-1-k}\phi_k\right),$$

$$\begin{aligned}\widehat{R}_g^m(\eta) = {} & g''_{m-1}(\eta) + \left(1 + M^2\beta_1\right)\sum_{k=0}^{m-1}\left(f_{m-1-k}g''_k + g_{m-1-k}g''_k\right) - \sum_{k=0}^{m-1} g_{m_{-1-k}}{}'g'_k, \\ & +2\beta_1\sum_{k=0}^{m-1} f_{m-1-k}\sum_{l=0}^{k} g_{k-l}{}'g''_l + 2\beta_1\sum_{k=0}^{m-1} g_{m-1-k}\sum_{l=0}^{k} g_{k-l}g''_l - m, \\ & \beta_1\sum_{k=0}^{m-1} g''_{m-1-k}\sum_{l=0}^{k} f_{k-1}f_l - \beta_1\sum_{k=0}^{m-1} g''_{m-1-k}\sum_{l=0}^{k} g_{k-1}f + 2\beta_1\sum_{k=0}^{m-1} g_{m-1-k}{}''\sum_{l=0}^{k} g_{k-1}g_l +, \\ & 2\beta_1\sum_{k=0}^{m-1} f''_{m-1-k}g''_k + 2\beta_1\sum_{k=0}^{m-1} g''_{m-1-k}g''_k - \beta_2\sum_{k=0}^{m-1} f_{m-1-k}g'''_k - \beta_2\sum_{k=0}^{m-1} g_{m-1-k}g'''_k - \left(\delta + M^2\right)g_{m-1}(\eta),\end{aligned} \tag{30}$$

$$\begin{aligned}\widehat{R}_\theta^m(\eta) = {} & \left(1 + \frac{4}{3}R_d\right)\theta''_{m-1}(\eta) + Pr\sum_{k=0}^{m-1}\left(f_{m-1-k}\theta'_k + g_{m-1-k}\theta'_k\right) - Pr\sum_{k=0}^{m-1} f_{m-1-k}{}'\theta'_k, \\ & -Pr * \varepsilon_t f_{m-1}{}'(\eta) + Pr * N_t\sum_{k=0}^{m-1}\theta_{m-1-k}{}'\theta'_k + Pr * N_b\sum_{k=0}^{m-1}\phi_{m-1-k}{}'\theta'_k + A^*\left(1 - \varepsilon_t\right)f_{m-1}{}'(\eta) + B^*\theta_{m-1}(\eta),\end{aligned} \tag{31}$$

$$\begin{aligned}\widehat{R}_\phi^m(\eta) = {} & \phi''_{m-1}(\eta) + Le * Pr\sum_{k=0}^{m-1}\left(f_{m-1-k}\phi'_k + g_{m-1-k}\phi'_k\right) - Le * Pr\sum_{k=0}^{m-1} f'_{m_{-1-k}}\phi_k, \\ & -Le * Pr * \varepsilon_c * f_{m-1}{}'(\eta) - Le * Pr * \gamma * \phi_{m-1}(\eta) - \gamma * Le * Pr * k_c\sum_{k=0}^{m-1}\phi_{m-1-k}\phi_k + \left(\frac{N_t}{N_b}\right)\theta''_{m-1}(\eta),\end{aligned} \tag{32}$$

$$\chi_m = \begin{cases} 0, & m \le 1, \\ 1, & m > 1. \end{cases} \tag{33}$$

The general solutions $f_m$, $g_m$, $\theta_m$, and $\phi_m$ of (23)–(26) with regard to particular solutions $f_m^*, g_{m'}^*\theta_m^*, \phi_m^*$ are expressed by

$$f_m(\eta) = f_m^*(\eta) + C_1 + C_2e^{\eta} + C_3e^{-\eta}, \tag{34}$$

$$g_m(\eta) = g_m^*(\eta) + C_4 + C_5e^{\eta} + C_6e^{-\eta}, \tag{35}$$

$$\theta_m(\eta) = \theta_m^*(\eta) + C_7e^{\eta} + C_8e^{-\eta}, \tag{36}$$

$$\phi_m(\eta) = \phi_m^*(\eta) + C_9e^{\eta} + C_{10}e^{-\eta}. \tag{37}$$

The general constants $C_i\,(i = 1 - 10)$ in the above equations are calculated by applying boundary conditions and are stated as

$$\left.\begin{aligned} & C_1 = C_2 = C_5 = C_7 = C_9, C_3 = \frac{\partial f_m^*(\eta)}{\partial\eta}|_{\eta=0} && C_1 = -C_3 - f_m^*(0), C_6 = \frac{\partial g_m^*(\eta)}{\partial\eta}|_{\eta=0} \\ & C_4 = -C_6 - g_m^*(0), \; C_1 = -C_3 - f_m^*(0) && C_8 = -\theta_m^*(0), C_{10} = -\phi_m^*(0) \end{aligned}\right\}. \tag{38}$$

## 4. Convergence Analysis

The admissible range for unknown boundary restrictions is the first task to obtain the solution via homotopy analysis method. This range can be traced by identifying those portions of curves lying exactly parallel to the horizontal axis as sketched in Figure 2. The solid-green line curve expresses $f''(0)$ with admissible range of $-0.7 \le \hbar_f \le -0.1$. The admissible range for the curve of $g''(0)$ is $-0.8 \le \hbar_g \le -0.1$, and it is depicted by the black dashed line. Similarly, the admissible ranges of $\theta'(0)$ and $\phi'(0)$ are estimated as $-0.6 \le \hbar_\theta \le -0.1$ and $-0.4 \le \hbar_\phi \le -0.1$, and they are represented by red and blue curves, respectively. For convenience, throughout the analysis we have chosen $\hbar_f = \hbar_g = \hbar_\phi = \hbar_\theta = -0.3 = \hbar$. Hence, the convergence table for appropriate amounts of emerging parameters is generated, and the corresponding results are shown through Table 1. Table 1 illustrates that at least sixty-four orders of approximation are needed to obtain the missing boundary conditions for $\theta(\eta)$ and $\phi(\eta)$, whereas at least seventy orders of approximation are required to attain the momentum boundary conditions. To maintain the convergence and

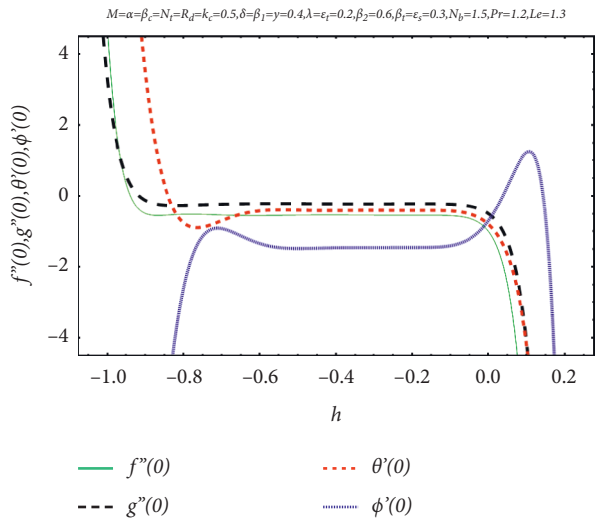


Figure 2: Estimation of convergent region via $\hbar$-curve sketching.

Table 1: Convergence check of series solutions by considering different orders of deformation $m$ when $\hbar = -0.3$ with the values of involved parameters kept the same as Figure 1.

| $m$ | $-f''(0)$ | $-g''(0)$ | $-\theta'(0)$ | $-\phi'(0)$ |
|---|---|---|---|---|
| 1 | 0.67180 | 0.33000 | 0.60480 | 0.99566 |
| 8 | 0.54487 | 0.22133 | 0.41078 | 1.45734 |
| 16 | 0.54294 | 0.22897 | 0.40751 | 1.45982 |
| 22 | 0.54220 | 0.22546 | 0.41026 | 1.46269 |
| 28 | 0.54556 | 0.22697 | 0.40922 | 1.45788 |
| 34 | 0.54160 | 0.22788 | 0.40893 | 1.46162 |
| 40 | 0.54399 | 0.22506 | 0.41025 | 1.46070 |
| 46 | 0.54236 | 0.22702 | 0.41048 | 1.46132 |
| 52 | 0.54311 | 0.22688 | 0.41057 | 1.46149 |
| 58 | 0.54286 | 0.22697 | 0.41065 | 1.46158 |
| 64 | 0.54292 | 0.22692 | 0.41067 | 1.46159 |
| 70 | 0.54288 | 0.22695 | 0.41067 | 1.46159 |
| 80 | 0.54288 | 0.22695 | 0.41067 | 1.46159 |

stability of the solution, the numbers of approximations are increased up to eight.

## 5. Results and Discussion

This section describes the graphical illustrations of temperature fluctuation, concentration fluctuation, local Nusselt number, and local Sherwood number under the consequences of important involved parameters. Figure 3 explains the impact of thermal stratification parameter $0 \le \varepsilon_t \le 1$ on dimensionless temperature fluctuation when the similarity variable is increased from $\eta = 0$ to $\eta = 4$ with the constant choices of other involved parameters. Maximum temperature fluctuation occurs at $\varepsilon_t = 0$, minimum temperature fluctuation is achieved at $\varepsilon_t = 1$, and thermal stratification phenomenon is generated for $0 < \varepsilon_t < 1$. Temperature profile is reduced with the improvement in the choice of $\varepsilon_t$. Physically, higher choice of $\varepsilon_t$ develops the ambient temperature and reduces the temperature at the surface. As a result, the temperature profile is reduced. The thickness of thermal layer is improved with the improvement in the value of the similarity variable. Figure 4 illustrates the trend of solutal stratification parameter $0 \le \varepsilon_s \le 1$ on dimensionless concentration fluctuation when the similarity variable is increased from $\eta = 0$ to $\eta = 1.8$ with the fixed amounts of other influential parameters. Maximum concentration is achieved at $\varepsilon_s = 0$, minimum concentration is obtained at $\varepsilon_s = 1$, and solutal stratification phenomenon is traced for $0 < \varepsilon_s < 1$. Concentration setup is diminished with the higher estimation of $\varepsilon_s$. The physical reason behind this outcome is the downfall of nanoparticle concentration at the wall and improvement of nanoparticle concentration away from the stretching device. Concentration layer thickness is also increased with the improvement of the similarity variable.

Figure 5 indicates the role of space-dependent heat source/sink parameter $-1.5 \le A^* \le 1.5$ in dimensionless temperature fluctuation with the increase of the similarity variable from $\eta = 0$ to $\eta = 8$. Minimum temperature is attained for heat consumption case, $-1.5 \le A^* < 0 - 1.5 \le A^* < 0$; maximum temperature is achieved for heat generation case, $0 < A^* \le 1.50 < A^* \le 1.5$; and moderate temperature is reached in the absence of heat

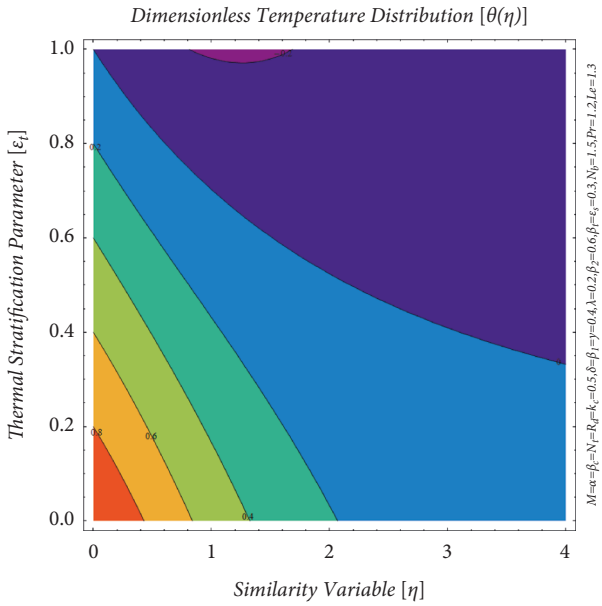


Figure 3: Interference of $\varepsilon_t$ on thermal layer $\theta(\eta)$.

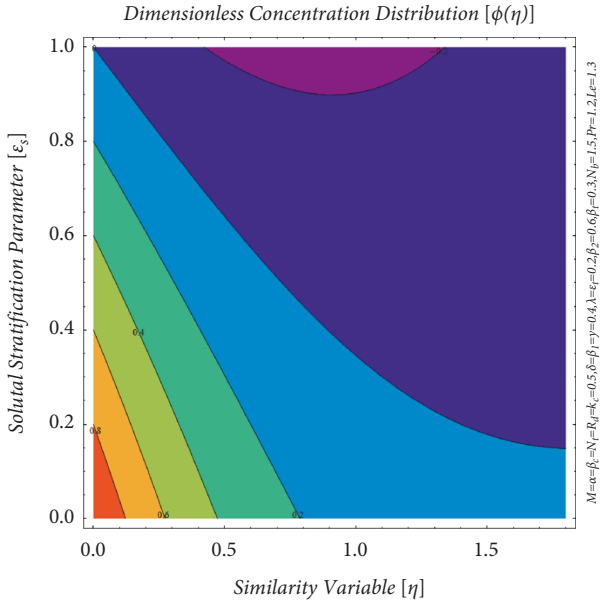


Figure 4: Interference of $\varepsilon_s$ on concentration layer $\phi(\eta)$.

generation/consumption, $A^* = 0$. Mathematically, $A^*$ is involved as a multiple of velocity profile $f'(\eta)$ in (7); therefore, the velocity profile also increases with the higher estimation of $A^*$, and hence temperature profile is improved. Therefore, it is called space-dependent heat source/sink influence on thermal profile. The thickness of thermal layer is also improved with the growth of the similarity variable. Figure 6 illuminates the potential of temperature-dependent heat source/sink parameter $-1.5 \le B^* \le 1.5$ on dimensionless temperature fluctuation with the growth of the similarity variable from $\eta = 0$ to $\eta = 8$. Minimal temperature is accomplished for heat ingestion case, $-1.5 \le B^* < 0 - 1.5 \le B^* < 0$; maximal temperature is realized for heat production case, $0 < B^* \le 1.50 < B^* \le 1.5$; and modest temperature is touched in the nonappearance of heat production/consumption, $B^* = 0$. Precisely, $B^*$ is involved as a multiple of $\theta(\eta)$ in (7); therefore, the thermal profile is also augmented with the greater estimation of $B^*$, and hence it is called temperature-dependent heat source/sink influence on thermal profile. The depth of thermal layer is also enriched with the progress of similarity variable. Figure 7 establishes the connection between dimensionless concentration fluctuation and chemical reaction parameter $0 \le k_c \le 20$ with the growth of the similarity variable up to $\eta = 3.2$. Decreasing trend in concentration fluctuation is observed with the growth in the estimation of $k_c$, maximal concentration is achieved for smaller values of $k_c$, and minimal concentration is generated for greater estimations of $k_c$. Physically, higher estimation of $k_c$ increases the second-order chemical reaction and reduces the first-order chemical reaction at the same time. As an outcome, negative trend in the concentration profile is attained. The thickness of concentration layer is also developed with the improvement in the similarity variable. Figure 8 explores the effect of thermal radiation parameter $0 \le R_d \le 4$ on thermal fluctuation with the evolution of the similarity variable from $\eta = 0$ to $\eta = 7$. A huge improvement in the thermal fluctuation is attained with the intensification in $R_d$. Maximal temperature is measured for higher $R_d$, and minimal temperature is obtained for basic/lower $R_d$. The thickness of thermal layer is also improved and it is found to be higher for the middle values of $R_d$. Physically, radiation is basically the transference of energy in the form of electromagnetic waves. More electromagnetic waves are produced with the improvement of $R_d$, and hence dominant temperature fluctuation is observed when $R_d$ reaches maximal estimation. Figure 9(a) deals with the relationship between relaxation time Deborah number $0 \le \beta_1 \le 10$ and temperature distribution for the similarity variable $0 \le \eta \le 7$. Here, thermal environment is upgraded with the higher estimation of $\beta_1$. Basically, $\beta_1$ is generated in the momentum equation due to the inclusion of Oldroyd-B nanoparticles and defined as the product of expansion rate $a$ and the relaxation time $\lambda_1$. Hence, higher estimation of $\beta_1$ enhances the value of $\lambda_1$ as well as the expansion rate. As an outcome, improvement in thermal setup is noticed with the upgraded width of thermal layer. Figure 9(b) shows the effect of $\beta_1$ on concentration fluctuation. Concentration is tremendously promoted with the advanced values of $\beta_1$. Physically, upgraded value of $\beta_1$ enhances the expansion rate that increases the movement of Oldroyd-B nanoparticles, and so concentration setup is boosted. Figure 10(a) establishes the link between retardation time Deborah number $0 \le \beta_2 \le 4$ and thermal fluctuation for the similarity variable $0 \le \eta \le 4$. At this time, thermal environment is degraded with the refined approximation of $\beta_2$. Fundamentally, $\beta_2$ involves in the momentum equation due to the presence of Oldroyd-B nanoparticles and is defined as the mathematical product of the stretching rate $a$ and the retardation time $\lambda_2$. Therefore, estimation of $\beta_2$ augments the value of $\lambda_2$ as well as the expansion rate. As a conclusion, reduction in thermal setup is perceived with the

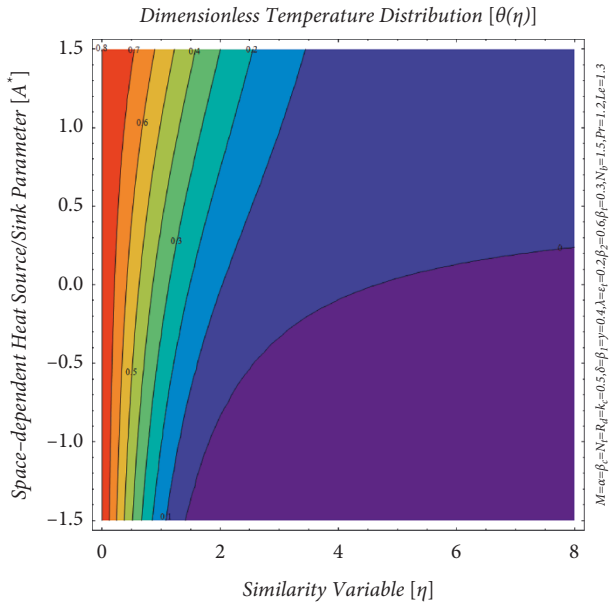


Figure 5: Interference of $A^*$ on thermal layer $\theta(\eta)$.

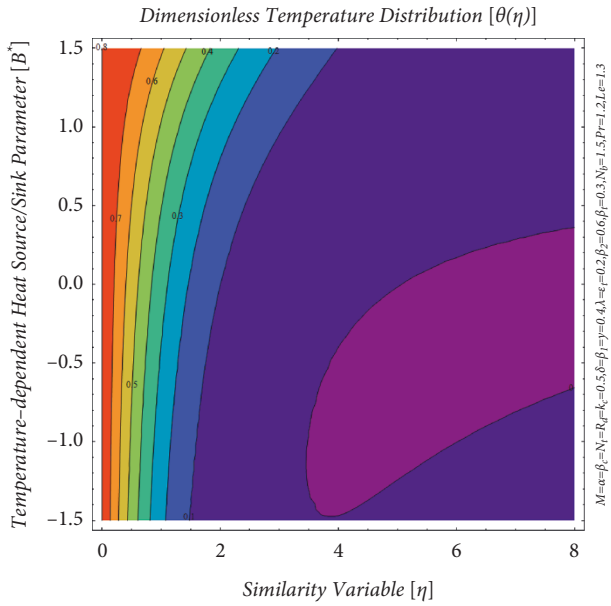


Figure 6: Interference of $B^*$ on thermal layer $\theta(\eta)$.

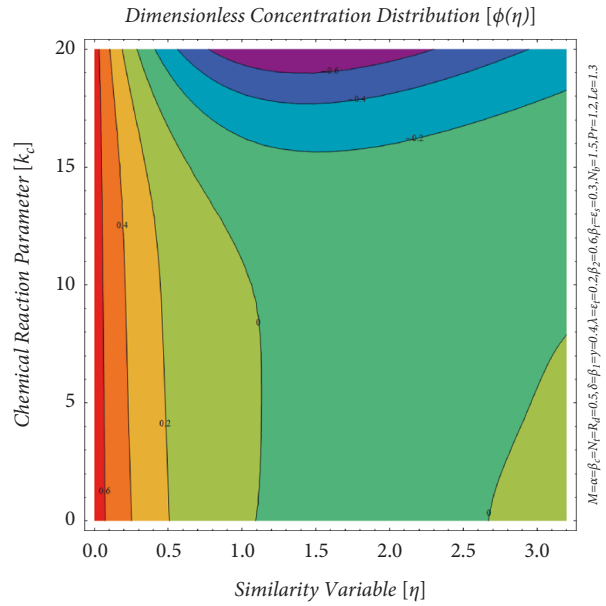


Figure 7: Interference of $k_c$ on concentration layer $\phi(\eta)$.

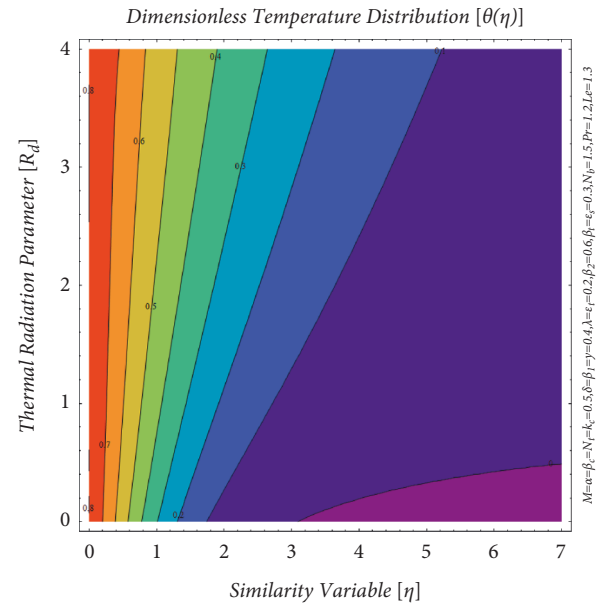


Figure 8: Interference of $R_d$ on thermal layer $\theta(\eta)$.

progressive width of thermal stream. Figure 10(b) illustrates the influence of $\beta_2$ on concentration flux. Concentration is enormously decreased with the advancement of $\beta_2$. Actually, improved value of $\beta_2$ develops the retardation rate, and so concentration setup is reduced.

Nusselt number measures the rate of heat transference whereas Sherwood number measures the rate of mass transference from hot region to cold region. Figure 11 describes the rate of heat transport with the combined inspiration of random motion $0 \le N_b \le 3$ and thermodiffusion $0 \le N_t \le 5$ parameters. Rate of heat transport is declined with the upgraded amounts of these parameters related to the nanofluid. Maximal rate of heat transport is measured for smaller amounts of these nanoparticle parameters, whereas minimal rate of heat transport is attained for greater amounts of $N_b$ and $N_t$. Maximum value of Nusselt number is approximated as 1.2, whereas minimum value of Nusselt number is estimated as 0.3 for the adopted ranges of Brownian and thermodiffusion parameters. Physically, a higher value of $N_b$ enhances the Brownian diffusion coefficient, and a higher value of $N_t$ enhances the thermodiffusion coefficient, whereas kinematic viscosity of Oldroyd-B nanofluid is reduced with the escalation of these parameters. As a whole, these physical changes are the main

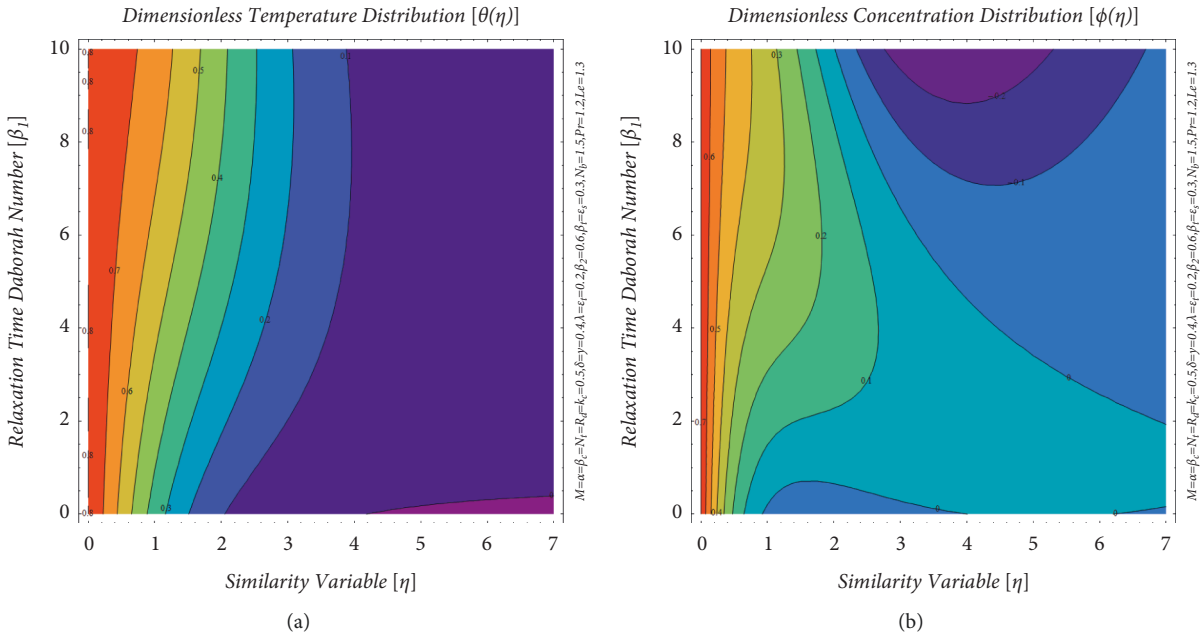


(a) (b)

Figure 9: (a) Interference of $\beta_1$ on thermal layer $\theta(\eta)$. (b) Interference of $\beta_t$ on concentration layer $\phi(\eta)$.

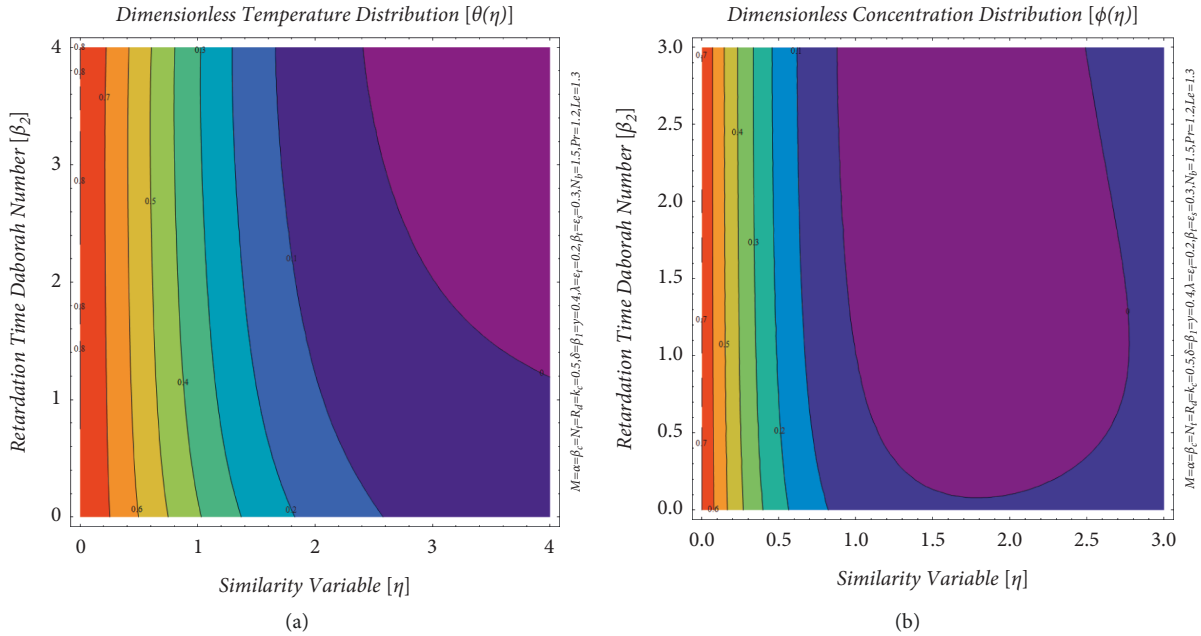


(a) (b)

Figure 10: (a) Interference of $\beta_2$ on thermal layer $\theta(\eta)$. (b) Interference of $\beta_2$ on concentration layer $\phi(\eta)$.

causes for the reduction of heat transport. Figure 12 shows the rate of mass transport with the collective stimulation of random motion $0 \le N_b \le 1$ and thermodiffusion $0 \le N_t \le 6$ parameters. Rate of mass transport is degenerated with the progress in the amount of $N_t$, whereas it is improved with the advancement in the amount of $N_b$. Highest rate of mass transport is stated for smaller choice of $N_t$ and higher choice of $N_b$. Maximum value of Sherwood number is formulated as 1.4, whereas minimum value of Sherwood number is predicted as −0.4 for the implemented ranges of Brownian and thermodiffusion factors. Physically, a higher value of $N_b$ enhances the heat capacity induced by nanoparticles, and a higher value of $N_t$ develops the temperature difference, whereas density of Oldroyd-B nanofluid is upgraded with the intensification of these forces. Overall, these physical variations are the main reasons for the improvement of Sherwood number with the positive tendency in $N_b$ and reduction of Sherwood number with the positive

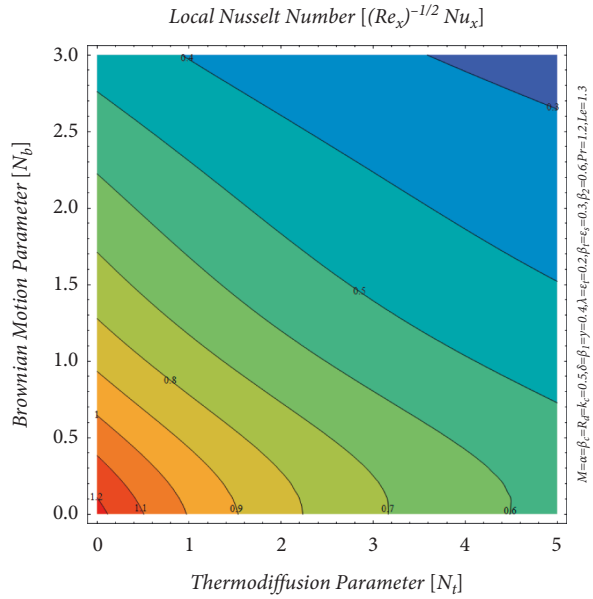


Figure 11: Nusselt number in the view of $N_b$ and $N_t$.

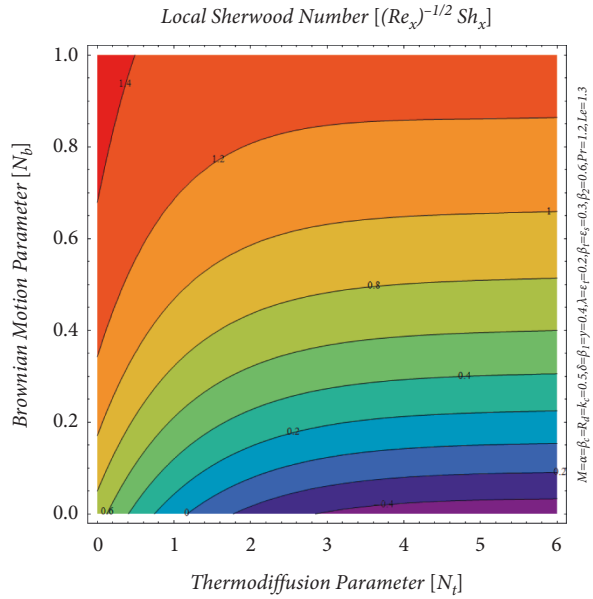


Figure 12: Sherwood number in the view of $N_b$ and $N_t$.

approach of $N_t$. Figure 13(a) indicates the rate of heat transport with the communal effect of thermal convection parameter $0 \le \beta_t \le 100$ and concentration convection parameter $0 \le \beta_c \le 100$. The maximum value of heat transport is reported as 0.84 for smaller communal effect of convection parameters, whereas the minimum value of heat transport is calculated as 0.7 for larger communal effect of convection parameters. Nusselt number is reduced with the higher estimation of $\beta_c$, and it is improved with the growth of $\beta_t$. On the other hand, Figure 13(b) explains the rate of mass transport with the combined effect of convection parameters. Sherwood number is improved with the estimation of $\beta_t$, and it is reduced with the growth of $\beta_c$. Maximum mass transport is observed at the right top of the figure and minimal mass transport is noticed at the left bottom of the figure. Physically, thermal convection parameter depends on the temperature difference, and thermal environment is reduced with its escalation; hence, rate of heat transport is improved. Moreover, concentration convection parameter relies on the concentration difference, and thermal environment is boosted with its growth; hence, rate of heat transport is reduced for this situation.

Table 2 is arranged to compare the present outcomes with the previously published work in the absence of

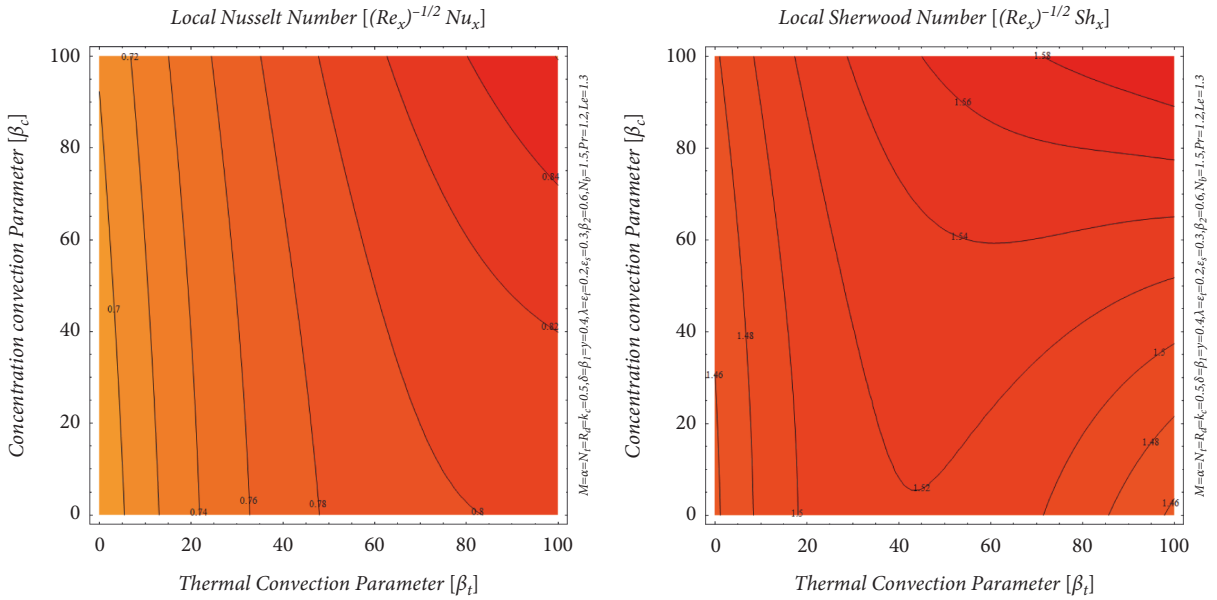


(a) (b)

Figure 13: (a) Nusselt number in the view of $\beta_t$ and $\beta_c$. (b) Sherwood number in the view of $\beta_t$ and $\beta_c$.

Table 2: Comparison establishment with the previously published report of Azeem Khan et al. [44] for $\delta = M = \lambda = \beta_t = \beta_c = A^* = \varepsilon_t = \varepsilon_s = R_d = \gamma = k_r = 0$.

| $\alpha$ | $Pr$ | $B^*$ | $N_b$ | $N_t$ | $Le$ | Present outcomes | | Published outcomes [44] | |
|---|---|---|---|---|---|---|---|---|---|
| | | | | | | $-\theta'(0)$ | $-\phi'(0)$ | $-\theta'(0)$ | $-\phi'(0)$ |
| 0.0 | 1.2 | 0.2 | 0.1 | 0.1 | 1.0 | 0.351853 | 0.474210 | 0.351853 | 0.474210 |
| 0.3 | | | | | | 0.509837 | 0.482838 | 0.509837 | 0.482838 |
| 0.4 | | | | | | 0.549438 | 0.488939 | 0.549438 | 0.488939 |
| 0.5 | 1.0 | | | | | 0.513728 | 0.430930 | 0.513728 | 0.430930 |
| | 1.1 | | | | | 0.551238 | 0.463216 | 0.551238 | 0.463216 |
| | 1.3 | | | | | 0.617393 | 0.527723 | 0.617393 | 0.527723 |
| | | 0.0 | | | | 0.757208 | 0.356670 | 0.757208 | 0.356670 |
| | | 0.1 | | | | 0.676907 | 0.422143 | 0.676907 | 0.422143 |
| | | 0.4 | | | | 0.335390 | 0.690221 | 0.335390 | 0.690221 |
| | | | 0.2 | | | 0.540514 | 0.683362 | 0.540514 | 0.683362 |
| | | | 0.3 | | | 0.497586 | 0.745281 | 0.497586 | 0.745281 |
| | | | 0.4 | | | 0.456841 | 0.775726 | 0.456841 | 0.775726 |
| | | | | 0.2 | | 0.575795 | 0.199343 | 0.575795 | 0.199343 |
| | | | | 0.4 | | 0.505394 | 0.277762 | 0.505394 | 0.277762 |
| | | | | 0.5 | | 0.480757 | 0.464410 | 0.480757 | 0.464410 |
| | | | | | 0.8 | 0.591165 | 0.352548 | 0.591165 | 0.352548 |
| | | | | | 0.9 | 0.588200 | 0.426414 | 0.588200 | 0.426414 |
| | | | | | 1.1 | 0.583427 | 0.560578 | 0.583427 | 0.560578 |

porosity, magnetic environment, dual stratifications, radiation, chemical reaction, and space-dependent heat source/sink factors. The reduced results for thermal and concentration gradients are best matched with the previously published report by Khan et al. [47] via homotopy analysis method.

## 6. Conclusions

The significance of higher-order chemical reaction and nonuniform heat source/sink influence on the dynamics of Oldroyd-B nanoparticles have been analytically investigated in this contribution. For physical relevancy, thermal radiation, mixed convection, and double stratification have also been incorporated in the bidirectional flow of the nanoliquid with the help of Buongiorno nanofluid model. Chief findings/outcomes of the ongoing exploration are listed below:

(i) Level of heat exposure is improved with the intensification in thermal stratification parameter $\varepsilon_t$, whereas level of mass exposure is reduced with

the improvement in solutal stratification parameter $\varepsilon_s$.

(ii) Level of mass exposure is developed with the higher selections of Brownian motion $N_b$ and chemical reaction $k_r$ parameters, whereas level of heat exposure is condensed with the escalation in the choices of heat source/sink parameters $A^*$&$B^*$ and radiation factor $R_d$.

(iii) Nusselt and Sherwood numbers are decreased with greater amounts of concentration convection parameter, whereas opposite trend is noticed for thermal convection parameter.

(iv) Higher estimations of Brownian and thermodiffusion parameters reduce the rate of heat transport.

(v) Temperature and concentration profiles are reduced with the positive tendency of retardation time Deborah number $\beta_2$, and opposite trends are detected for relaxation time Deborah number $\beta_1$.

Finally, the outcomes obtained through this investigation are helpful in the improvement of thermal instruments. This mathematical model has some applications in biomedicine and chemical and mechanical engineering like coating a sheet with nanomaterial, paper production process, and treatment of cancer.

## Data Availability

The raw data supporting the conclusion of this paper will be made available by the corresponding author without undue reservation.

## Conflicts of Interest

The authors declare that they have no conflicts of interest.

## Authors' Contributions

All authors contributed equally to this work and read and approved the final version of the paper.

## References

[1] S. U. Choi and J. A. Eastman, "Enhancing thermal Conductivity of Fluids with Nanoparticles," in *Proceedings of the 1995 International mechanical engineering congress and exhibition*, Argonne National Lab., IL (United States), San Francisco, CA, USA, November 1995.

[2] Y. Xuan and Q. Li, "Heat transfer enhancement of nanofluids," *International Journal of Heat and Fluid Flow*, vol. 21, no. 1, pp. 58–64, 2000.

[3] J. Buongiorno, "Convective transport in nanofluids," *Journal of Heat Transfer*, vol. 128, no. 3, pp. 240–250, 2006.

[4] B. C. Sakiadis, "Boundary-layer behavior on continuous solid surfaces: I. Boundary-layer equations for two-dimensional and axisymmetric flow," *AIChE Journal*, vol. 7, no. 1, pp. 26–28, 1961.

[5] L. J. Crane, "Flow past a stretching plate," *Zeitschrift für angewandte Mathematik und Physik ZAMP*, vol. 21, no. 4, pp. 645–647, 1970.

[6] C. Y. Wang, "The three-dimensional flow due to a stretching flat surface," *Physics of Fluids*, vol. 27, no. 8, pp. 1915–1917, 1984.

[7] P. D. Ariel, "Generalized three-dimensional flow due to a stretching sheet," *Zamm*, vol. 83, no. 12, pp. 844–852, 2003.

[8] M. Sajid and T. Hayat, "Influence of thermal radiation on the boundary layer flow due to an exponentially stretching sheet," *International Communications in Heat and Mass Transfer*, vol. 35, no. 3, pp. 347–356, 2008.

[9] W. A. Khan and I. Pop, "Boundary-layer flow of a nanofluid past a stretching sheet," *International Journal of Heat and Mass Transfer*, vol. 53, no. 11-12, pp. 2477–2483, 2010.

[10] K. Bhattacharyya and G. C. Layek, "Chemically reactive solute distribution in MHD boundary layer flow over a permeable stretching sheet with suction or blowing," *Chemical Engineering Communications*, vol. 197, no. 12, pp. 1527–1540, 2010.

[11] I. Ahmad, M. Ahmed, Z. Abbas, and M. Sajid, "Hydromagnetic flow and heat transfer over a bidirectional stretching surface in a porous medium," *Thermal Science*, vol. 15, no. 2, pp. 205–220, 2011.

[12] I. C. Liu and H. I. Andersson, "Heat transfer over a bidirectional stretching sheet with variable thermal conditions," *International Journal of Heat and Mass Transfer*, vol. 51, no. 15-16, pp. 4018–4024, 2008.

[13] W. Ibrahim and O. D. Makinde, "The effect of double stratification on boundary-layer flow and heat transfer of nanofluid over a vertical plate," *Computers & Fluids*, vol. 86, pp. 433–441, 2013.

[14] K. Loganathan, S. Sivasankaran, M. Bhuvaneswari, and S. Rajan, "Second-order slip, cross-diffusion and chemical reaction effects on magneto-convection of Oldroyd-B liquid using Cattaneo-Christov heat flux with convective heating," *Journal of Thermal Analysis and Calorimetry*, vol. 136, no. 1, pp. 401–409, 2019.

[15] N. Sandeep and M. G. Reddy, "MHDOldroyd-B fluid flow across a melting surface with cross diffusion and double stratification," *The European Physical Journal Plus*, vol. 132, no. 3, pp. 1–18, 2017.

[16] M. Waqas, M. Ijaz Khan, T. Hayat, and A. Alsaedi, "Stratified flow of an Oldroyd-B nanoliquid with heat generation," *Results in Physics*, vol. 7, pp. 2489–2496, 2017.

[17] M. Turkyilmazoglu and I. Pop, "Heat and mass transfer of unsteady natural convection flow of some nanofluids past a vertical infinite flat plate with radiation effect," *International Journal of Heat and Mass Transfer*, vol. 59, pp. 167–171, 2013.

[18] M. M. Rashidi, S. Abelman, and N. Freidooni Mehr, "Entropy generation in steady MHD flow due to a rotating porous disk in a nanofluid," *International Journal of Heat and Mass Transfer*, vol. 62, pp. 515–525, 2013.

[19] A. Moradi, A. Alsaedi, and T. Hayat, "Investigation of nanoparticles effect on the jeffery-hamel flow," *Arabian Journal for Science and Engineering*, vol. 38, no. 10, pp. 2845–2853, 2013.

[20] O. D. Makinde, W. A. Khan, and Z. H. Khan, "Buoyancy effects on MHD stagnation point flow and heat transfer of a nanofluid past a convectively heated stretching/shrinking sheet," *International Journal of Heat and Mass Transfer*, vol. 62, pp. 526–533, 2013.

[21] B. Mahanthesh, B. J. Gireesha, S. A. Shehzad, F. M. Abbasi, and R. S. R. Gorla, "Nonlinear three-dimensional stretched flow of an Oldroyd-B fluid with convective condition, thermal radiation, and mixed convection," *Applied Mathematics and Mechanics*, vol. 38, no. 7, pp. 969–980, 2017.

[22] A. K. Ghosh and P. Sana, "On hydromagnetic flow of an Oldroyd-B fluid near a pulsating plate," *Acta Astronautica*, vol. 64, no. 2-3, pp. 272–280, 2009.

[23] S. Mukhopadhyay, "Effects of slip on unsteady mixed convective flow and heat transfer past a porous stretching surface," *Nuclear Engineering and Design*, vol. 241, no. 8, pp. 2660–2665, 2011.

[24] R. Kandasamy, I. Muhaimin, and A. K. Rosmila, "The performance evaluation of unsteady MHD non-Darcy nanofluid flow over a porous wedge due to renewable (solar) energy," *Renewable Energy*, vol. 64, pp. 1–9, 2014.

[25] R. S. Tripathy, G. C. Dash, S. R. Mishra, and S. Baag, "Chemical reaction effect on MHD free convective surface over a moving vertical plate through porous medium," *Alexandria Engineering Journal*, vol. 54, no. 3, pp. 673–679, 2015.

[26] A. Ali, H. Zaman, M. Z. Abidin, and S. I. A. Shah, "Analytic solution for fluid flow over an exponentially stretching porous sheet with surface heat flux in porous medium by means of homotopy analysis method," *American Journal of Computational Mathematics*, vol. 05, no. 02, pp. 224–238, 2015.

[27] B. S. Goud, "MHD flow past a vertical oscillating plate with radiation and chemical reaction in porous medium-finite difference method," *International Journal of Emerging Trends in Engineering Research*, vol. 5, no. 11, pp. 32–35, 2017.

[28] M. Faisal, I. Ahmad, and T. Javed, "Numerical assessments of prescribed heat sources on unsteady 3D flow of Williamson nanoliquid through porous media," *Special Topics & Reviews in Porous Media - An International Journal*, vol. 12, no. 2, pp. 71–92, 2021.

[29] P. Besthapu, R. U. Haq, S. Bandari, and Q. M. Al-Mdallal, "Mixed convection flow of thermally stratified MHD nanofluid over an exponentially stretching surface with viscous dissipation effect," *Journal of the Taiwan Institute of Chemical Engineers*, vol. 71, pp. 307–314, 2017.

[30] I. Ahmad, M. Faisal, and T. Javed, "Unsteady rotating flow of nanofluid with prescribed thermal aspects," *International Journal of Modern Physics C*, vol. 32, no. 7, pp. 1–18, 2021.

[31] T. S. Karthik, K. Loganathan, A. N. Shankar et al., "Zero and nonzero mass flux effects of bioconvective viscoelastic nanofluid over a 3D riga surface with the swimming of gyrotactic microorganisms," *Advances in Mathematical Physics*, vol. 2021, Article ID 9914134, 13 pages, 2021.

[32] T. Hayat, M. Z. Kiyani, I. Ahmad, and A. Alsaedi, "Double stratified radiative flow of an Oldroyd-B nanofluid with nonlinear convection," *Applied Mathematics and Mechanics*, vol. 40, no. 12, pp. 1861–1878, 2019.

[33] I. Ahmad, M. Faisal, and T. Javed, "Dynamics of copper-water nanofluid with the significance of prescribed thermal conditions," *Heat Transfer*, vol. 50, no. 5, pp. 4248–4263, 2021.

[34] M. Faisal, I. Ahmad, and T. Javed, "Keller-Box simulation for nonzero and zero mass fluxes of nanofluid flow impinging over a bi-directional stretching sheet: an unsteady mathematical model," *International Journal of Modern Physics C*, vol. 32, no. 4, Article ID 2150052, 2021.

[35] G. Sarojamma, R. Vijaya Lakshmi, K. Sreelakshmi, and K. Vajravelu, "Dual stratification effects on double-diffusive convective heat and mass transfer of a sheet-driven micropolar fluid flow," *Journal of King Saud University Science*, vol. 32, no. 1, pp. 366–376, 2020.

[36] D. Srinivasacharya and O. Surender, "Effect of double stratification on mixed convection boundary layer flow of a nanofluid past a vertical plate in a porous medium," *Applied Nanoscience*, vol. 5, no. 1, pp. 29–38, 2015.

[37] I. Ahmad, I. Khurshid, M. Faisal, T. Javed, and Z. Abbas, "Mixed convective flow of an Oldroyd-B nanofluid impinging over an unsteady bidirectional stretching surface with the significances of double stratification and chemical reaction," *SN Applied Sciences*, vol. 2, no. 9, pp. 1–14, 2020.

[38] K. Loganathan, K. Mohana, M. Mohanraj, P. Sakthivel, and S. Rajan, "Impact of third-grade nanofluid flow across a convective surface in the presence of inclined Lorentz force: an approach to entropy optimization," *Journal of Thermal Analysis and Calorimetry*, vol. 144, no. 5, pp. 1935–1947, 2020.

[39] M. Faisal, I. Ahmad, and T. Javed, "Dynamics of MHD tangent hyperbolic nanofluid with prescribed thermal conditions, random motion and thermo-migration of nanoparticles," *Journal of Dispersion Science and Technology*, pp. 1–15, 2021.

[40] K. Loganathan and S. Rajan, "An entropy approach of Williamson nanofluid flow with Joule heating and zero nanoparticle mass flux," *Journal of Thermal Analysis and Calorimetry*, vol. 141, pp. 2599–2612, 2020.

[41] I. Ahmad, M. Faisal, and T. Javed, "Magneto-nanofluid flow due to bidirectional stretching surface in a porous medium," *Special Topics & Reviews in Porous Media - An International Journal*, vol. 10, no. 5, pp. 457–473, 2019.

[42] T. Hayat, T. Muhammad, S. A. Shehzad, M. S. Alhuthali, and J. Lu, "Impact of magnetic field in three-dimensional flow of an Oldroyd-B nanofluid," *Journal of Molecular Liquids*, vol. 212, pp. 272–282, 2015.

[43] I. Ahmad, M. Faisal, and T. Javed, "Unsteady flow of Walters-B magneto-nanofluid over a bidirectional stretching surface in a porous medium with heat generation," *Special Topics & Reviews in Porous Media - An International Journal*, vol. 12, no. 3, pp. 49–70, 2021.

[44] W. Azeem Khan, M. Khan, and R. Malik, "Three-dimensional flow of an Oldroyd-B nanofluid towards stretching surface with heat generation/absorption," *PLoS One*, vol. 9, no. 8, Article ID e105107, 2014.

[45] I. Ahmad, M. Faisal, T. Javed, and I. L. Animasaun, "Insight into the relationship between unsteady Cattaneo-Christov double diffusion, random motion and thermo-migration of tiny particles," *Ain Shams Engineering Journal*, vol. 13, 2021.

[46] S. Asghar, M. Jalil, M. Hussan, and M. Turkyilmazoglu, "Lie group analysis of flow and heat transfer over a stretching rotating disk," *International Journal of Heat and Mass Transfer*, vol. 69, pp. 140–146, 2014.

[47] M. Turkyilmazoglu, "Nanoliquid film flow due to a moving substrate and heat transfer," *The European Physical Journal Plus*, vol. 135, no. 10, pp. 1–13, 2020.

[48] I. Ahmad, M. Faisal, T. Javed, A. Mustafa, and M. Z. Kiyani, "Numerical investigation for mixed convective 3D radiative flow of chemically reactive Williamson nanofluid with power law heat/mass fluxes," *Ain Shams Engineering Journal*, vol. 13, 2021.

[49] J. A. Khan, M. Mustafa, T. Hayat, M. Turkyilmazoglu, and A. Alsaedi, "Numerical study of nanofluid flow and heat transfer over a rotating disk using Buongiorno's model," *International Journal of Numerical Methods for Heat and Fluid Flow*, vol. 27, no. 1, pp. 221–234, 2017.

[50] M. Turkyilmazoglu, "On the transparent effects of Buongiorno nanofluid model on heat and mass transfer," *The European Physical Journal Plus*, vol. 136, no. 4, pp. 1–15, 2021.